Fabrication of fully aligned self-assembled cell-laden collagen filaments for tissue engineering *via* a hybrid bioprinting process

JuYeon Kim [a], Hyeongjin Lee [b], Gyudo Lee [b], Dongryeol Ryu [c], GeunHyung Kim [a,*]

[a] *Department of Precision Medicine, Sungkyunkwan University School of Medicine (SKKU-SOM), Suwon, 16419, Republic of Korea*
[b] *Department of Biotechnology and Bioinformatics, Korea University, Sejong, Republic of Korea*
[c] *Department of Biomedical Science and Engineering, Gwangju Institute of Science and Technology, Gwangju, Republic of Korea*

A B S T R A C T

Cell-laden structures play a pivotal role in various tissue engineering applications, particularly in tissue restoration. Interactions between cells within bioprinted structures are crucial for successful tissue development and regulation of stem cell fate through intricate cell-to-cell signaling pathways. In this study, we developed a new technique that combines polyethylene glycol (PEG)-infused submerged bioprinting with a stretching procedure. This approach facilitated the generation of fully aligned collagen structures consisting of myoblasts and a low concentration (2 wt%) of collagen to efficiently encourage muscle tissue regeneration. By adjusting several processing parameters, we obtained biologically safe and mechanically stable cell-laden collagen filaments with uniaxial alignment. Notably, the cell filaments exhibited markedly elevated cellular activities compared to those exhibited by conventional bioprinted filaments, even at similar cell densities. Moreover, when we implanted structures containing adipose stem cells into mice, we observed a significantly increased level of myogenesis compared to that in normally bioprinted struts. Thus, this promising approach has the potential to revolutionize tissue engineering by fostering enhanced cellular interactions and promoting improved outcomes in regenerative medicine.

1. Introduction

Muscle tissue engineering and regenerative medicine have emerged as critical domains for addressing the challenges posed by muscle injury and degenerative conditions. The development of advanced strategies to promote muscle regeneration requires the integration of biomaterial science and tissue engineering principles [1–5].

Three-dimensional (3D) bioprinting has recently emerged as a promising technology for fabricating cell-laden structures for various tissue-engineering applications, including muscle regeneration. However, normal bioprinting processes frequently require high concentrations of hydrogel bioink to ensure the mechanical stability of 3D bioconstructs with uniquely designed physical cues [5–8]. Recently, various bioprinting strategies including extrusion, inkjet, laser-assisted, and vat photopolymerization and electrospinning process were combined into a hybrid bioprinting system to obtain highly complex tissues (Supplementary Table S1) [9–22]. However, this reliance on high concentrations of bioink can inadvertently impede efficient cellular activities, including cell proliferation and differentiation, within the 3D cell construct. Conversely, precise cellular alignment within the bioink matrix is an imperative factor in the successful regeneration of aligned human tissues, including muscle tissue; however, low concentrations of hydrogel-based bioink typically fail to induce efficient cellular alignment. This failure can be attributed to the relatively low viscosity as a result of an extrusion-based bioprinting process, which cannot sustain the predesigned cell alignment attained by the external forces owing to low mechanical sustainability [23].

To overcome the shortcomings of current bioinks, composite bioinks using bioactive materials such as collagen or decellularized extracellular matrix as the matrix phase and leachable biomaterials (gelatin, alginate, and synthetic hydrogels, such as poly(ethylene glycol) (PEG)) as the dispersed phase have been investigated [24,25]. Although composite bioinks can provide a solution for the initial poor mechanical properties of printed cell-laden structures, cell loss during leaching and poor mechanical properties after leaching still pose issues [26]. Amongst various biomaterials, collagen has been widely implemented for bioprinting

processes for its bioactivities, as illustrated by various applications detailed in Supplementary Table S2 [26–48]. For instance, methacrylated bioinks (e.g., methacrylated collagen and gelatin) have been used to overcome the poor mechanical properties of cell-laden structures fabricated using an optical crosslinking process. Nevertheless, the ultraviolet light and photoinitiators, such as lithium phenyl-2,4, 6-trimethylbenzoylphosphinate and irgacure, added to the bioinks can have potentially toxic effects on laden cells [43]. Furthermore, non-homogeneous crosslinking degree in a radial direction of the printed struts can pose challenges in the use of the optical crosslinking process [7].

To induce efficient cell alignment that can be used for various aligned tissue structures, several studies attempting to align various cell types, including fibroblasts, myoblasts, and cardiac cells, using electromechanical devices and functional biomaterials, have been conducted. These methods include light-assisted cell alignment using TiO2 nanodots and methacrylated gelatin (GelMA) [49], extrusion devices with patterned grooves or nozzles [7,50], acoustic myoblast patterning in a GelMA bioink [51], magnetically active hydrogels [52], *in situ* electric field-assisted bioprinting [53–55], and sacrificing poly(vinyl alcohol) with aligned patterns [4]. While these techniques have shown excellent results in promoting cell alignment and myofibril formation for muscle tissue regeneration, they often require specialized equipment, complex processes, and unique biomaterial compositions.

To overcome these challenges, we present a new methodology for the fabrication of uniaxially aligned cell-laden microfibers using a low concentration ($\sim$2 wt%) of collagen bioink, which offers a transformative approach to enhance muscle tissue regeneration. In this study, we introduce a new system that combines PEG-filled submerged bioprinting with a stretching process similar to the conventional wet fiberspinning process. When collagen hydrogel structures are immersed in a PEG solution, the PEG molecules interact with water molecules present in collagen owing to their high affinity for water, and it effectively draws water out of the collagen hydrogel through a process called "osmosis." This results in the removal of a significant portion of water within the collagen structure. As water is extracted from collagen, the density of the packed collagen molecules increases, inducing a non-covalent crosslinking called physical crosslinking, similar to that in the dehydrothermal crosslinking process [56,57]. This densification of collagen is often desirable in tissue engineering because it can improve the mechanical properties and structural integrity of the constructs.

Similar to that in previous studies, the incorporation of PEG within the bath medium induces the dehydration of extruded struts of a low weight fraction of collagen hydrogel, facilitating the formation of densely packed fibrillated collagen structures. The concentration and molecular weight of the PEG solution in the bath significantly affect the viability of the resulting dehydrated protein constructs [58]. Through cautious selection of PEG solution factors, mechanically stable myoblast (or human adipose stem cell, hASC)-laden collagen constructs can be obtained.

In addition, using a stretching process, the cells laden in the dehydrated collagen construct were manipulated into a uniaxially aligned cell structure. Furthermore, by subjecting the extruded cell-laden collagen struts to controlled stretching, we observed the mechanotransduction effects of the laden cells, which ensured efficient remodeling of the surrounding extracellular matrix (ECM). This phenomenon promotes actin fiber formation and myogenesis for enhanced muscle regeneration [59]. To evaluate the translational viability of our engineered muscle constructs, we carried out *in vivo* implantation studies using a mouse model with volumetric muscle loss (VML). The results showed a significant restoration of muscle function and robust muscle regeneration.

Through the incorporation of a low-weight fraction collagen bioink, precise cellular alignment, and mechanotransduction-mediated cellular responses, we offer a transformative solution that significantly impacts the advancement of muscle regeneration strategies. Based on these results, the combined process (bioprinting combined with PEG-induced dehydration and stretching) provides a new promising platform to fabricate aligned tissue structures.

2. Results and discussion

2.1. Fabrication of collagen hydrogel using a PEG fibrillation process

In terms of biological effects, an appropriate weight fraction of the hydrogel matrix in various bioinks is essential for various tissue-regeneration applications [60]. This characteristic allows the creation of cell constructs that closely mimic the natural extracellular matrix, thereby facilitating effective cell interactions. Such an environment promotes improved cell migration, proliferation, and differentiation within the hydrogel, while also enabling the efficient diffusion of essential nutrients and oxygen [61]. However, maintaining complex 3D cell constructs with unique physical properties, including topographical cues, can be challenging with the use of low-concentration collagen bioink ($\sim$2 wt%) owing to its poor mechanical properties.

To address this issue, we employed a PEG-assisted gelation process to prepare a collagen bioink. Traditionally, collagen hydrogels have been gelled using two common methods: (1) physical methods, involving fibrillogenesis through variations in temperature, collagen concentration, pH, and assistance of PEG and (2) chemical crosslinking, which employs agents such as glycation, genipin, carbodiimide hydrochloride (EDC)/N-hydroxysuccinimide (NHS), glutaraldehyde, and multi-armed PEG [62,63]. We used a physical gelation process that involved the dehydration of PEG to efficiently remove water molecules without inducing collagen denaturation or posing a toxic threat to cells. PEG functions as a nonreactive solvent absorber, swiftly eliminating water molecules from the pregel collagen solution while promoting intramolecular bonding (amide bonds) among the collagen molecules, thereby facilitating physical gelation, as shown in Fig. 1A [56,64].

Fig. 1B–D illustrate the schematic of the gelation mechanism and the optical and scanning electron microscopy (SEM)/atomic force microscopy (AFM) images of collagen hydrogels (2 wt%) cross-linked chemically with EDC/NHS and fibrillated using temperature (37 °C, Temp-fibrillation) and PEG (M_w = 6000 g/mol and 50 wt%, PEG-fibrillation) at 37 °C. Optical images clearly showed phase-separated collagen in the PEG solution, whereas phase separation of the collagen solution was not observed for EDC/NHS crosslinking and temperature gelation of collagen. A comparison of the AFM images shown in Fig. 1D and Supplementary Fig. S1A shows that the fibrillated collagen was qualitatively clearer in the Temp-fibrillation and PEG-fibrillation processes than in the chemical-crosslinking process. However, fibrillated collagen showed a completely different structure for the Temp-fibrillation and PEG-fibrillation processes. In the AFM images, the collagen fibrils that developed during Temp-fibrillation process showed a relatively homogenous fibril diameter but with a non-fibrillated collagen component (approximately 13.3%, Supplementary Fig. S1B), as indicated by the AFM image (red arrow). However, the collagen fibrils processed by PEG-fibrillation showed a hierarchical structure consisting of two different sizes (D_1 and D_2, indicated by white arrows in the AFM image) of fibrils, and non-fibrillated collagen components were not observed. We carefully estimated the possibility of hierarchical structure formation because the addition of PEG can immediately generate homogeneous small-sized collagen fibrils, and the additional temperature fibrillation could gradually induce the formation of thicker collagen fibers. When comparing the diameters of the fibrillar collagen (Fig. 1E), the Temp-fibrillation induced a much greater collagen fibril diameter than PEG-fibrillation, but with a higher non-fibrillated component.

Additionally, the optical images presented in Supplementary Fig. S2A, along with corresponding videos, elucidate the qualitative assessment of the fibrillation degree in collagen struts subjected to media at 37 °C (video 1) and PEG solution (video 2). Approximately 10 s subsequent to elevating the collagen strut exposed to each solution, the
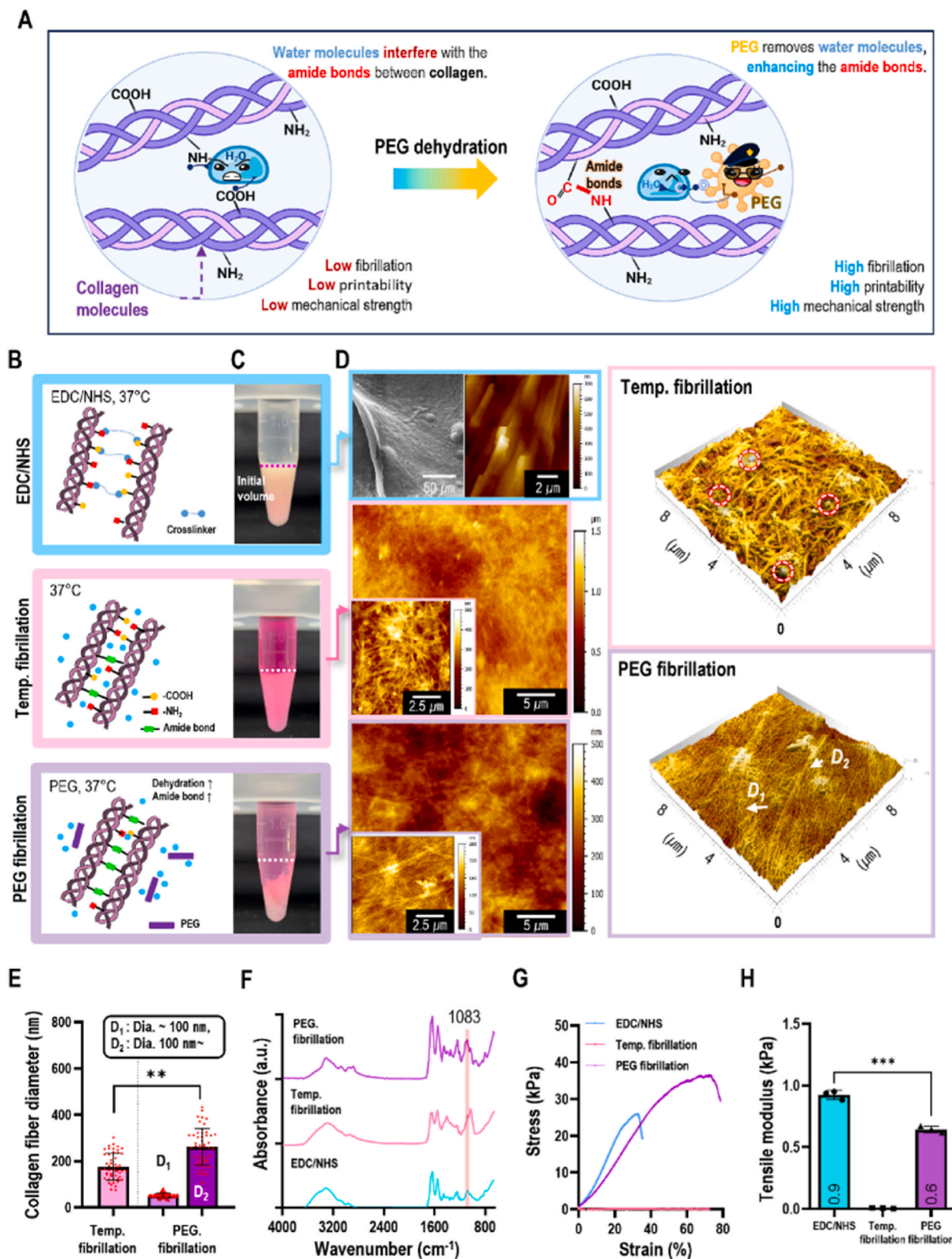
Fig. 1. (**A**) Schematic demonstrating the mechanism by which PEG induces dehydration effects on collagen fibrillation. (**B**) Schematic of chemical (EDC/NHS) and physical crosslinking (Temp.-fibrillation and PEG-fibrillation) mechanisms, (**C**) optical images of gelled collagen, (**D**) SEM/AFM images describing the surface morphology of gelled collagen and magnified 3D surface topographical images of 2 wt% collagen hydrogels that were gelled using temperature and PEG fibrillation. Red-dotted circles indicate non-fibrillated collagen component, and D_1 (small diameter, less than 100 nm, of collagen fibrils) and D_2 (large diameter, more than 100 nm, of collagen fibrils) demonstrate two different fibrillated collagen structures. (**E**) Measured diameter of collagen fibrils, (**F**) FT-IR spectra, (**G**) tensile stress-strain curves, and (**H**) measured tensile modulus of collagen structure crosslinked using various crosslinking conditions.

collagen immersed in the media displayed minimal fibrous formation. Conversely, the collagen within the PEG solution exhibited an obvious fibrillated collagen strut, enabling its manipulation with tweezers. Similarly, the stress-strain curves of the collagen construct treated with the PEG solution showed significant improvements in mechanical strength compared to the construct treated with the media (Supplementary Fig. S2B).

Supplementary video related to this article can be found at https://

Fourier transform infrared (FTIR) spectra were recorded to evaluate the degree of collagen fibrillation. According to Nashchekina et al., a peak with a wavenumber of 1083 cm^{-1} corresponding to the tensile vibrations of a bond of CO molecules indicates the formation of collagen fibrils [65]. Fig. 1F shows the IR spectra of collagen treated with EDC/NHS, Temp fibrillation, and PEG fibrillation. A significantly higher increase in the peak at 1083 cm^{-1} was observed in the spectrum of the
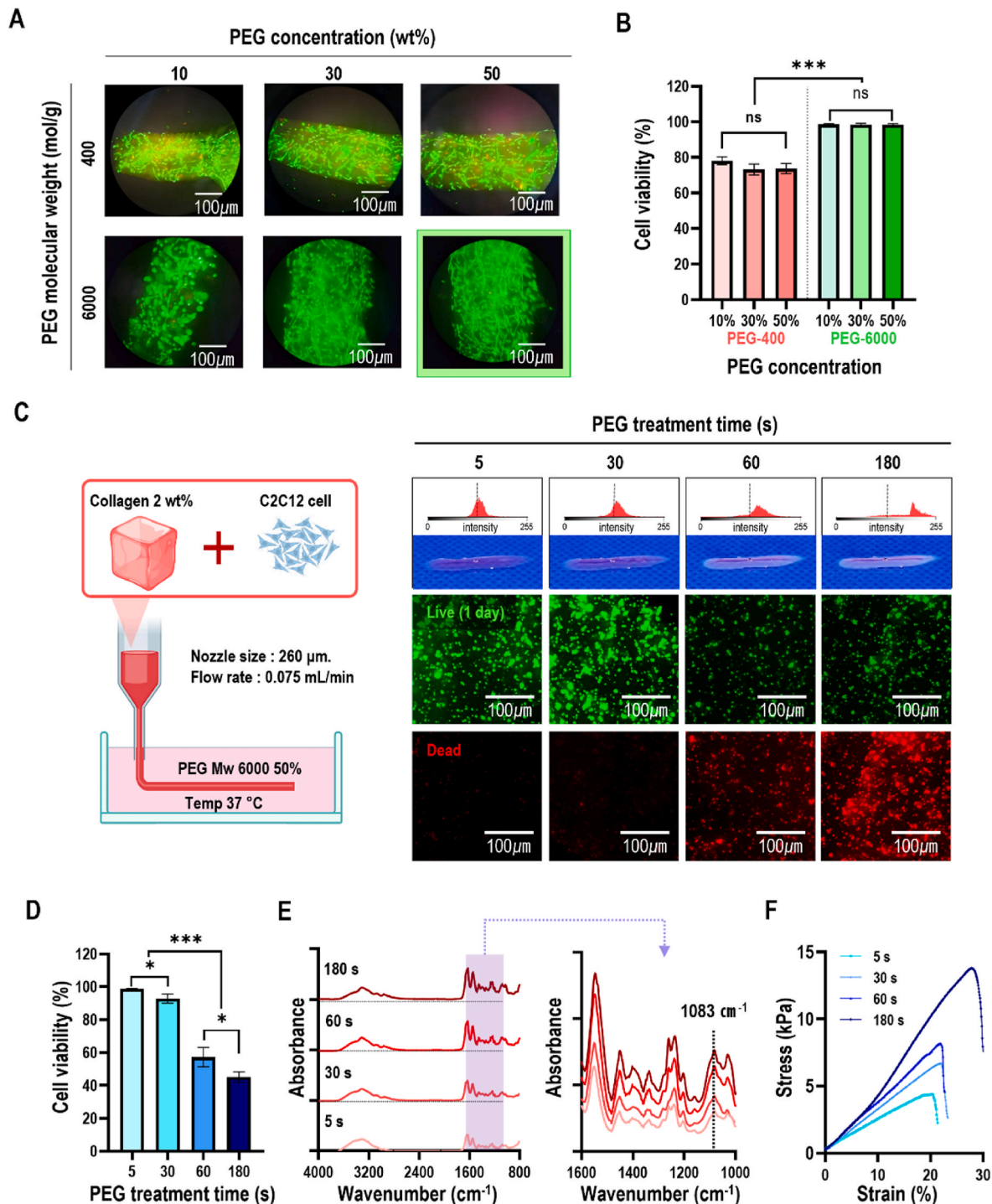

Fig. 2. (**A**) Live (green)/dead (red) images and (**B**) calculated cell viability of C2C12 cells in fibrillated collagen obtained using various PEG concentrations (10, 30, and 50 wt%) and molecular weights (400 and 6000 g/mol). (**C**) Schematic of cell-laden collagen hydrogel bioprinted in PEG-solution, and optical and live/dead images of C2C12 cells on day 1 for various PEG treatment times (5, 30, 60, and 180 s). (**D**) Calculated cell viability, (**E**) FT-IR spectra, and (**F**) tensile stress-strain curve of collagen structures with various PEG treatment times.

fibrillated collagen treated with PEG solution than in the spectrum of the Temp-fibrillated and chemically crosslinked collagen. The obtained spectra were in good agreement with the AFM results.

We also examined the mechanical properties of the three collagen structures after full drying, as these properties directly influence cytoskeletal formation in various cell types. Furthermore, the fibrillated collagen structure can affect cell remodeling, mechanical properties, cell-to-cell signaling, and cell polarization [66]. The tensile testing was performed using a universal testing machine (UTM), and it was observed that the chemically crosslinked collagen hydrogel exhibited significantly higher stiffness than that of the physically gelled collagen structures (Fig. 1G). The collagen fibrillated with a PEG solution demonstrated a significantly higher stiffness than that of the collagen treated only with Temp-fibrillation. This difference in stiffness can be attributed to the dependence of these properties on homogeneous and well-fibrillated collagen. Notably, an increase in the nonfibrillated component of collagen can result in reduced mechanical stiffness, whereas well-developed collagen fibrils can contribute to an overall increase in stiffness. This result aligns with those of previous studies, indicating that hierarchical fibrous structures have distinct effects on the mechanical properties of the material [67].

To prevent the temperature-induced fibrillation of collagen for bio-ink preparation, we treated the collagen solution at 22 °C (room temperature), given that collagen fibrillation did not occur at this temperature, as evidenced by the storage modulus, G' (Supplementary Fig. 3SA). The result was corroborated by SEM images, which reveal the absence of collagen fibrils in structures treated at 22 °C, contrasting with the presence of collagen fibrils in structures treated at 36 °C (Supplementary Fig. 3B).

PEG is recognized for its biocompatibility and ability to modify the physicochemical properties of biomolecules and materials. The molecular weight (MW) and concentration of PEG can significantly influence its interaction with cells and cell viability [58]. Lower molecular weight PEGs such as PEG (Mn ~ 200) are more likely to penetrate cell membranes, potentially affecting cell function and viability [58].

To observe the effects of PEG MW, concentration, and treatment time on the viability of the cells laden in collagen hydrogel, we used two PEG-MWs (M_w ~ 400 and 6000 g/mol), three concentrations (10, 30, and 50 wt%), and various PEG treatment times (5–180 s). To determine the effect of PEG MW and concentration (Fig. 2A), C2C12 cells were loaded onto collagen struts (2 wt%) in PEG solutions with a 5-s treatment time. In the live/dead images, the viability of cells in the PEG-400 solution was significantly lower than that in the PEG-6000 solution, and the cell viability was similar at various concentrations (Fig. 2B). However, high MW and concentration of PEG did not affect cell viability (Fig. 2B). Similar results have been reported in cytotoxic studies of PEG-based monomers, where a low-MW PEG-based solution (M_n ~ 500 g/mol) exhibited higher toxicity toward various cells, including fibroblasts, than a high PEG-MW solution (M_n ~ 950 g/mol) [58]. Similarly, increasing the concentration of low-MW PEG induced toxicity in cells. Based on previous work and our results, the low-MW PEG, PEG-400, exhibits higher cytotoxicity toward C2C12 cells than PEG-6000, although the specific cell type can also influence cytotoxic outcomes.

In addition, we measured the effect of PEG treatment time on cell viability at an M_w of 6000 g/mol and 50% concentration of PEG. Fig. 2C shows the optical and live/dead images for various PEG treatment times. Interestingly, the increase in PEG treatment time clearly induced collagen fibrillation, which was determined using color images from transparent to white (video 3) and caused toxicity to the laden cells; the cell-viability gradually decreased over 10 s (Fig. 2D). When the laden C2C12 cells were exposed to PEG-MW and PEG-concentration for a prolonged treatment time, the residual stress caused by the collagen fibers during the fibrillation process, which lasted for a long time, could cause significant damage to the cells intercalated between the collagen fibrils, eventually affecting the reduction of cell viability. In addition, the degree of collagen fibrillation, determined by the peak (1083 cm^{-1})

in the IR spectra and tensile properties, gradually increased with increasing treatment time (Fig. 2E and F, and Supplementary Fig. S4). To evaluate this hypothesis, we cultured the cells in the same PEG solution without loading them into the collagen solution (Supplementary Fig. S5A). As shown by the results in Figs. S3B and C, cell viability was not affected by the treatment time until 600 s.

Supplementary video related to this article can be found at https://doi.org/10.1016/j.bioactmat.2024.02.020

Thus, the PEG solution (PEG M_w = 6000 g/mol, concentration = 50%) and its treatment time (~10 s or less) for the process were set based on these results.

2.2. A uniaxially aligned cell-construct for muscle tissue engineering

Alignment of cells in artificial cell constructs plays an important role in muscle tissue regeneration [68]. This alignment is crucial for the integration of motor neurons with muscle cells, ultimately leading to improved control and coordination of muscle movements. In cases of muscle injury or degeneration, the use of uniaxially aligned cell constructs represents a promising approach for muscle repair and regeneration as it closely mimics the natural alignment of muscle fibers.

In this study, we propose a strategy that combines these two methods to create uniaxially aligned cell-laden collagen filaments (Fig. 3A). First, we employed submerged bioprinting, a 3D bioprinting technique in which the printing occurs underwater within a PEG solution (with M_w = 6000 g/mol, concentration of 50 wt%, and a treatment time less than 10 s). As demonstrated in the previous section, this approach could physically fibrillate the cell-laden collagen (at a concentration of 2 wt%). Second, we used a stretching process to align the cells within the extruded filaments along the stretching direction. The PEG and collagen concentration was determined by assessing the process diagram shown in Supplementary Fig. S6. It indicated a stable processing region at a collagen concentration of 2 wt% and a PEG concentration above 30 wt %.

During the submerged printing step, the cell-laden collagen bioink underwent rapid fibrillation upon contact with the PEG solution. Importantly, this process did not compromise the cell viability under the specified conditions. The hydrogel solution simultaneously provided support and maintained the structural integrity of the printed cell struts. Following initial printing, a stretching process was applied to the printed cell structure. This process involves subjecting printed filaments to mechanical forces that induce the alignment of cells and fibrillated collagen in a uniaxial direction. The stretching was achieved using mechanical devices such as a guided rotator and collector, as depicted in Fig. 3A and video 4.

Supplementary video related to this article can be found at https://doi.org/10.1016/j.bioactmat.2024.02.020

The stretching process plays a key role in achieving uniaxial alignment of cells laden in collagen filaments. Parameters such as the extrusion rate of the collagen bioink from the nozzle and the stretching speed significantly influence cell alignment and filament uniformity. An appropriately selected diagram of the stretching process is imperative to avoid unstable formation of cell filaments.

To determine the safe range of stretching parameters for stable cell-filament formation, the parameters were systematically manipulated. Fig. 3B illustrates the stable (O) and unstable (Δ and ×) filament formation ranges concerning the collagen flow rate from the nozzle and rotation speed, while maintaining a constant nozzle diameter (350 μm) and fixed concentrations of bioink (2 wt% collagen) and PEG (M_w = 6000 g/mol and 50%) in the bath. The choice of a 350 μm nozzle diameter was made because smaller nozzles, although capable of achieving finer filament alignment, may necessitate higher pressures, potentially causing cell damage during the extrusion process.

When the rotation speed of the collector and the collagen flow rate from the nozzle were too high, unstable filament formation was observed. This instability was attributed to the draw ratio of the collagen
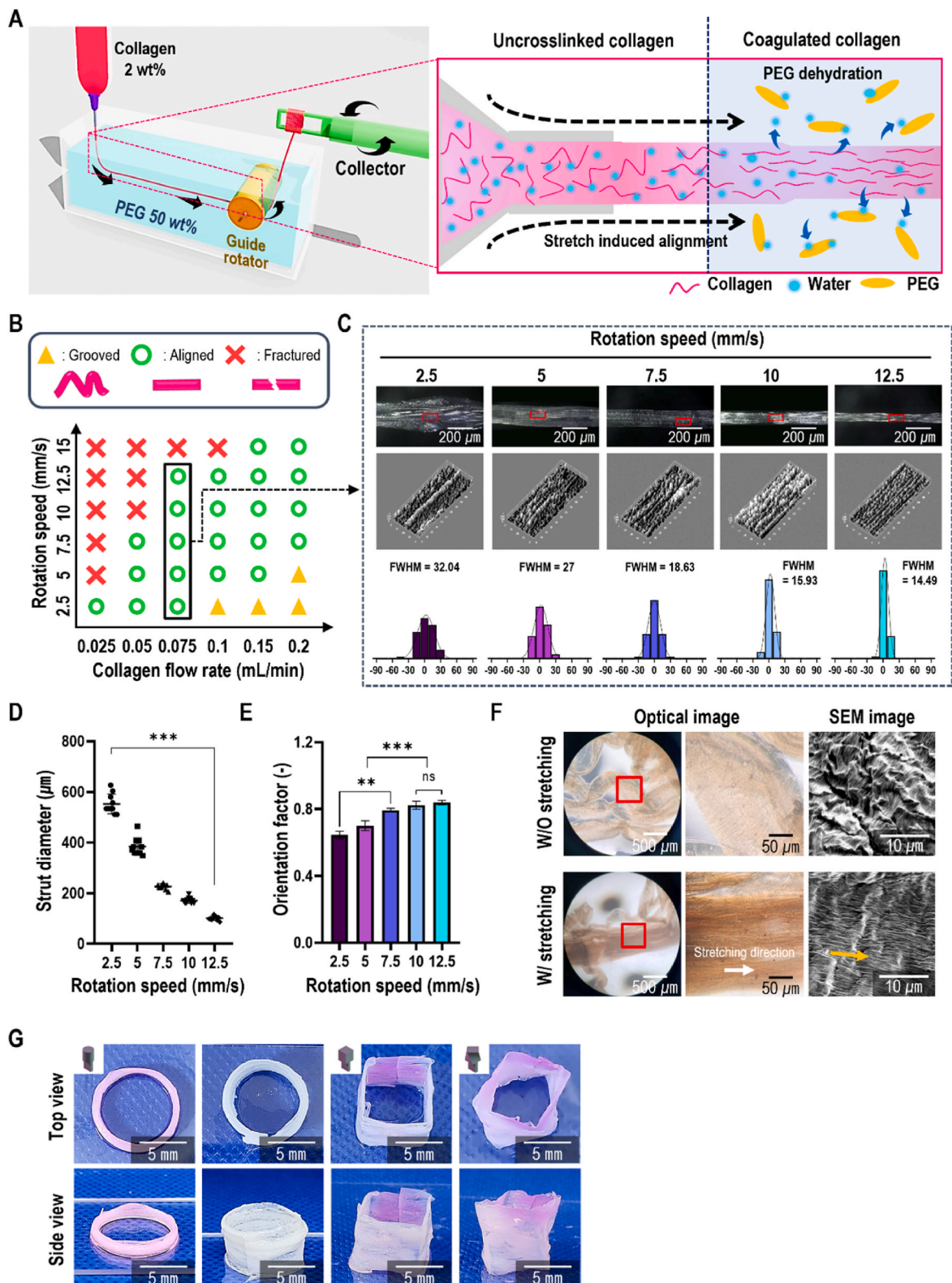
Fig. 3. (**A**) Schematic diagram illustrating the combined printing (C-printing) process with submerged bioprinting and stretching process. (**B**) Parameter process diagram for various rotation speeds of the collector (2.5–15 mm/s) and collagen flow rate (0.025–0.2 mL/min), and (**C**) optical image, 3D surface mapping, and histograms of orientation degree for various rotation speeds (2.5, 5, 7.5, 10, and 12.5 mm/s) with fixed collagen flow rate (0.075 mL/min). (**D**) Measured strut diameter and (**E**) orientation factor of collagen struts with various rotation speeds. (**F**) Optical and SEM images of collagen struts fabricated using only submerged bioprinting (w/o stretching) and combined printing (with stretching) systems. (**G**) Various cell-laden structures fabricated using the combined printing.

filament, which was either excessively high or low in the PEG solution. Additionally, smaller diameters of cell-laden filaments can promote cell alignment along the filament direction, which is crucial for certain tissue types, such as the muscle or nerve tissues. Conversely, excessively large-diameter cell-laden hydrogels may lead to reduced cell viability in the core region owing to the limitation of nutrient and oxygen diffusion [69]. Moreover, in our previous research, a diameter of 200 μm for cell-laden struts (composed of 3.5 wt% alginate and 1×10^6 cells/mL of MC3T3-E1 cells) yielded appropriate biological activities, including satisfactory cell viability and reasonable cellular functions [69]. However, it is worth noting that various factors such as the type and concentration of the hydrogel, cell type, and cell density can influence the suggested diameter.

Fig. 3C–E showed the diameter and orientation factor $(90^o - \varphi)/90^o$ of cell-laden filaments at various rotating speeds of the collector, where φ is the angle at full width at half maximum in the alignment distribution. As anticipated, the diameter exhibited a linear decrease as the rotation speed increased, while maintaining a constant collagen extrusion flow rate (0.075 mL/min) from the nozzle. In addition, an increase in rotation speed clearly induced the alignment of collagen fibrils (Fig. 3E). Based on these observations, we selected specific stretching conditions for the process, including a collagen flow rate of 0.075 mL/min, a rotating speed of 10 mm/s, and a cell-laden filament diameter of 201–220 μm.
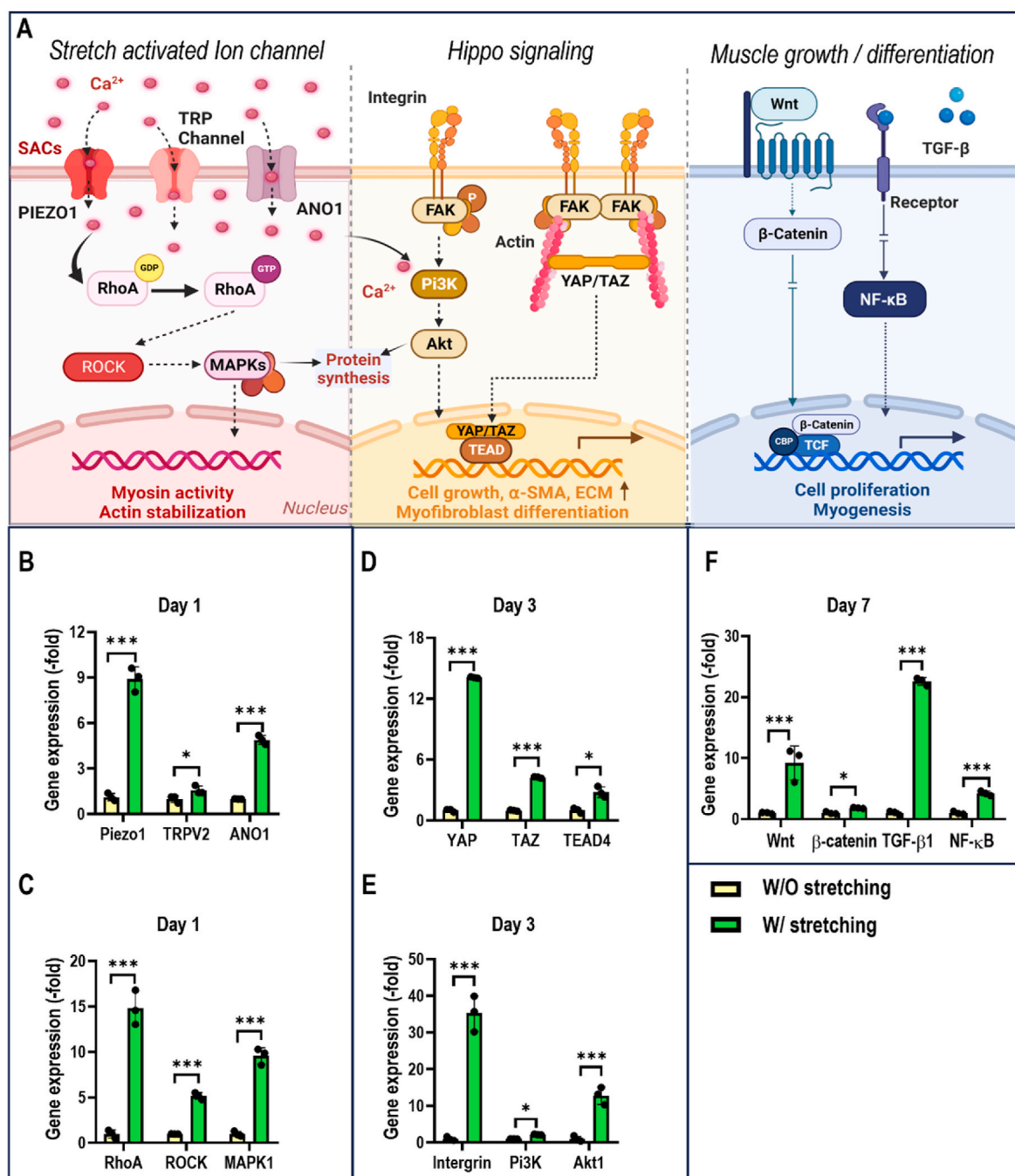

Fig. 4. (**A**) Schematic diagram of the mechanotransduction cell signaling pathways affecting various cellular activities. Relative gene expression related to (**B**, **C**) stretching-activated ion channels (Piezo1, TRPV2, ANO1, RhoA, ROCK, and MAPK1), (**D**, **E**) hippo signaling (YAP, TAZ, TEAD 4, Integrin, Pi3K, and Akt1), and (**F**) muscle growth/differentiation (Wnt, β-catenin, TGF-β1, NF-κB) in C2C12 cells cultured in bioconstruct fabricated using the PEG-assisted submerged printing with and without the stretching process.

Fig. 3F display optical and SEM images of the cell-filaments fabricated without and with the stretching process (collagen flow rate = 0.075 mL/min and rotating speed of the collector = 10 mm/s), respectively. In the optical images, physically stable strut formation was observed in both cases during the submersion process. Furthermore, optical and SEM images showed well-fibrillated collagen during both the processing conditions. However, SEM images clearly revealed uniaxial alignment of the fibrillated collagen for the stretched cell constructs, whereas the non-stretched cell constructs exhibited randomly distributed fibrillated collagen.

To better illustrate the hybrid printing method for creating diverse 3D structures, including a cylindrical shape resembling tracheal anatomy as depicted in Fig. 3G, we utilized cell-laden collagen bioink to fabricate these structures. The internal images within the figures showed collectors (both cylindrical and cubic in shape) used in the submerged bioprinting process, along with a side view of the fabricated structures. In addition, the wall thickness of the cylindrical structures can be controlled *via* the collection duration of the cell-laden collagen microfibers (Supplementary Fig. S7).

2.3. Mechanotransduction effect of the wet-stretching process

During stretching, along with the tension experienced by the fibrillated collagen, which acts as a topographical cue, the cells within the bioink also directly sense the change, inducing mechanotransduction. Mechanotransduction is the process by which cells sense and respond to mechanical forces, translating them into biochemical signals that can influence cellular behavior [70–73]. Mechanical stimulation can affect cell proliferation and differentiation because cells can respond to stretching by producing and remodeling the ECM, further influencing tissue structure and function [73].

To examine how cells respond to mechanical forces in a stretched collagen filament during the stretching process, we analyzed the genes associated with the mechanical stretching force, which can be transmitted through the ECM and neighboring cells, as depicted in Fig. 4A.

This stretching phenomenon can be detected by integrin receptors and mechanosensitive ion channels, including transient receptor protein ion channels and piezoelectric ion channels. This, in turn, triggers the activation of focal adhesion kinase (FAK) and a cascade of signaling pathways, including the RhoA/Rock, Wnt/β-catenin, MAPK, TGF-β, and Pi3K pathways. These pathways regulate various cellular responses, such as cell proliferation and cytoskeleton organization, and the expression of various myogenic genes. Specifically, the RhoA/Rock pathway promotes the formation of actin stress fibers, while the activated Wnt/β-catenin pathway enhances nuclear activity and gene expression. Conversely, the TGF-β pathway promotes NF-kB activation, which is instrumental in muscle growth and increased cellular proliferation.

To assess the impact of mechanical stretching on cells loaded within the stretching process, we examined the expression of genes associated with mechanotransduction 1, 3, and 7 days after cell culture. Our results indicated a substantial increase in gene expression in cell-laden filaments subjected to stretching compared to cell filaments fabricated only through extrusion. This suggests that the tensile forces exerted during the stretching process play an important role in reorganizing the cellular cytoskeleton (Fig. 4B and C) and cell growth (Fig. 4D) regulated by the activity of the Yes-associated protein (Yap) and transcriptional co-activator with the PDZ-binding motif (Taz), eventually promoting myogenesis and muscle growth (Fig. 4E and F).

Real-time polymerase chain reaction (RT-PCR) confirmed that the mechanical stretching clearly encouraged the growth and maturation of muscle cells.

2.4. In vitro myogenic activities of the stretched cell-laden collagen filaments

To evaluate the myogenic potential of C2C12 cells laden with stretched collagen filaments, we investigated myotube formation and the expression of myogenesis-related genes after various cell culture durations. During fabrication, we set the diameter of the cell-laden collagen filament as about 220 ± 14 μm because the diameter can directly affect nutrient and oxygen diffusion during the culture periods. Fig. 5A shows live/dead cells at 3 and 7 d, DAPI (blue)/phalloidin (red) staining images at 14 d, and DAPI/myosin heavy chain (MHC; green) staining images at 21 d for the two cell-laden collagen filaments, one subjected to (experimental) and the other not subjected to (control) stretching.

Live/dead images strongly indicated high cell viability (>90%) in both groups, confirming the safety of the proposed process for encapsulated cells (Fig. 5B). Moreover, consistent with previous observations of F-actin, cells within the stretched collagen filaments were notably stretched in the tensile direction (Fig. 5C). Most notably, the experimental group exhibited more evident myotube development, coupled with a significantly higher alignment of MHC, than the control group (Fig. 5D and E). Furthermore, the aligned structures within the experimental group demonstrated greater fusion (the number of nuclei within myotubes relative to the total number of nuclei) and maturation indices (the number of myotubes containing more than five nuclei relative to the total number of myotubes) than those of the control structures (Fig. 5F).

To evaluate myogenic genes in the stretched cell filaments, we explored the expression of myogenesis-related genes, specifically MyoG, MyoD, and MHC, at 21 d (Fig. 5G). In the experimental group, where C2C12 cells were subjected to mechanical stretching, expression of myogenic genes increased markedly compared to that in the control group. Thus, the upregulation of myogenic genes signifies effective induction of the myogenic lineage through mechanical stimulation of C2C12 cells.

2.5. Application of the proposed process to hASCs

To evaluate the combined printing process (C-printing; submerged bioprinting using a PEG solution and stretching) in hASCs, we conducted a comparative analysis with cell-laden filaments fabricated using normal bioprinting (N-printing) as a control. The bioink concentrations and processing conditions for each process are shown in Fig. 6A.

Fig. 6B shows the live/dead cells at 3 and 7 days, DAPI/phalloidin staining at 14 d, and DAPI/MHC staining images after 21 days for cell-laden collagen filaments processed with N-printing and C-printing systems. As shown, the cell viability and F-actin analysis results demonstrated that each process was safe for the laden cells (Fig. 6C). A significantly higher nucleus aspect ratio and more meaningful F-actin alignment were obtained for hASCs laden in the collagen constructs processed with C-printing than those processed with the N-printing process (Fig. 6D and E).

Similarly, the quantitative evaluation of MHC immunofluorescent staining *via* MHC positive area, fusion, and maturation index indicated significantly higher myogenic activities in hASCs cultured in bioconstructs fabricated using the C-printing method (Fig. 6F and G).

To observe the mechanotransduction effect of cell structures, we measured two typical genes (Piezo-1, which can regulate the regenerative capacity of skeletal muscle [74] and Taz, which is a modulator of myogenic differentiation and muscle regeneration [75,76] (Fig. 6H). As expected, the genes were significantly expressed in the filament fabricated during the C-printing process, indicating that the stretching process can affect myogenesis over much longer culture periods. We further evaluated the expression levels of genes related to myogenic differentiation (MHC and MyoD1) after 21 d of cell culture (Fig. 6H). As expected, in hASCs from the C-printing system, the expression levels of myogenic genes were enhanced compared to the gene levels in the
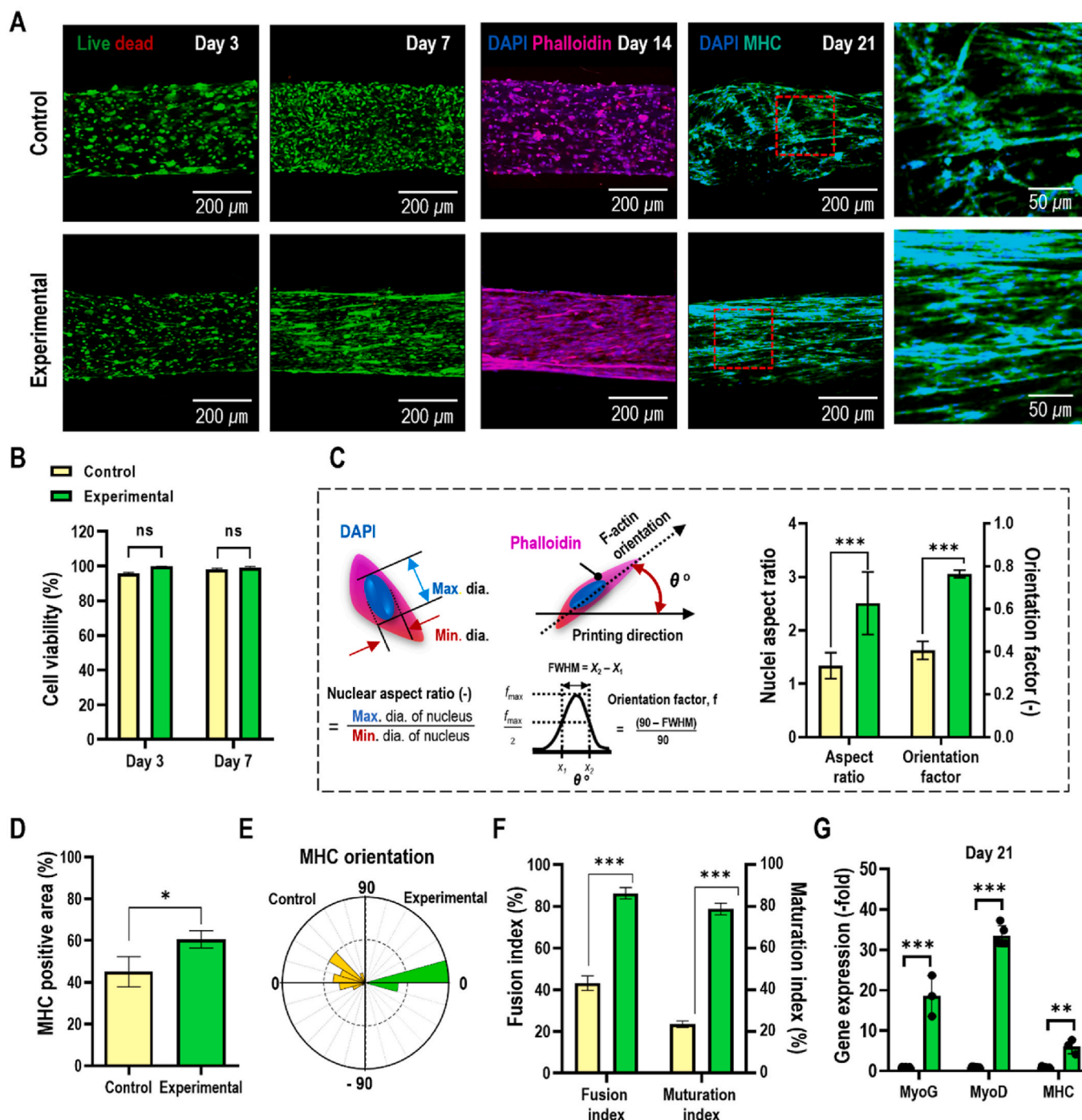
Fig. 5. (A) Live/dead (day 3 and 7), DAPI (blue)/phalloidin (red) staining (day 14), and DAPI (blue)/MHC (green) staining (day 21) images of C2C12 cells cultured in the cell-laden constructs fabricated using only submerged bioprinting (control) and combined bioprinting method (experimental). Measured (B) cell viability, (C) nucleus aspect ratio and orientation factor, (D) MHC-positive area, (E) MHC orientation distribution, and (F) MHC fusion and maturation index of cells cultured in control and experimental bioconstructs. (G) Relative expression levels of myogenesis-related genes of myogenin (Myog), myogenic differentiation 1 (MyoD), and myosin heavy chain (MHC).

hASCs from the N-printing system (2.7-fold higher for MHC and 3.2-fold higher for MyoD1).

Based on these results, we expect that the myogenesis of printed hASCs encapsulated within collagen filaments processed using C-printing will be clearly enhanced by the synergistic effect of mechanical stimulation due to tensile stretching during the process and the fully aligned topographical cues of the fibrillated collagen, in contrast to that in the control.

2.6. In vivo results of volumetric muscle model

The volumetric muscle model (VML) was established through surgical excision of the extensor digitorum longus/extensor hallucis longus muscles in mice, accompanied by a deliberate 40% loss of the tibialis anterior (TA) muscle. This process results in an irreversible volumetric deficiency. The collagen-based bioconstructs ($4 \times 2 \times 1.5$ mm^3) loaded with hASCs were prepared as shown in Supplementary Fig. S8.
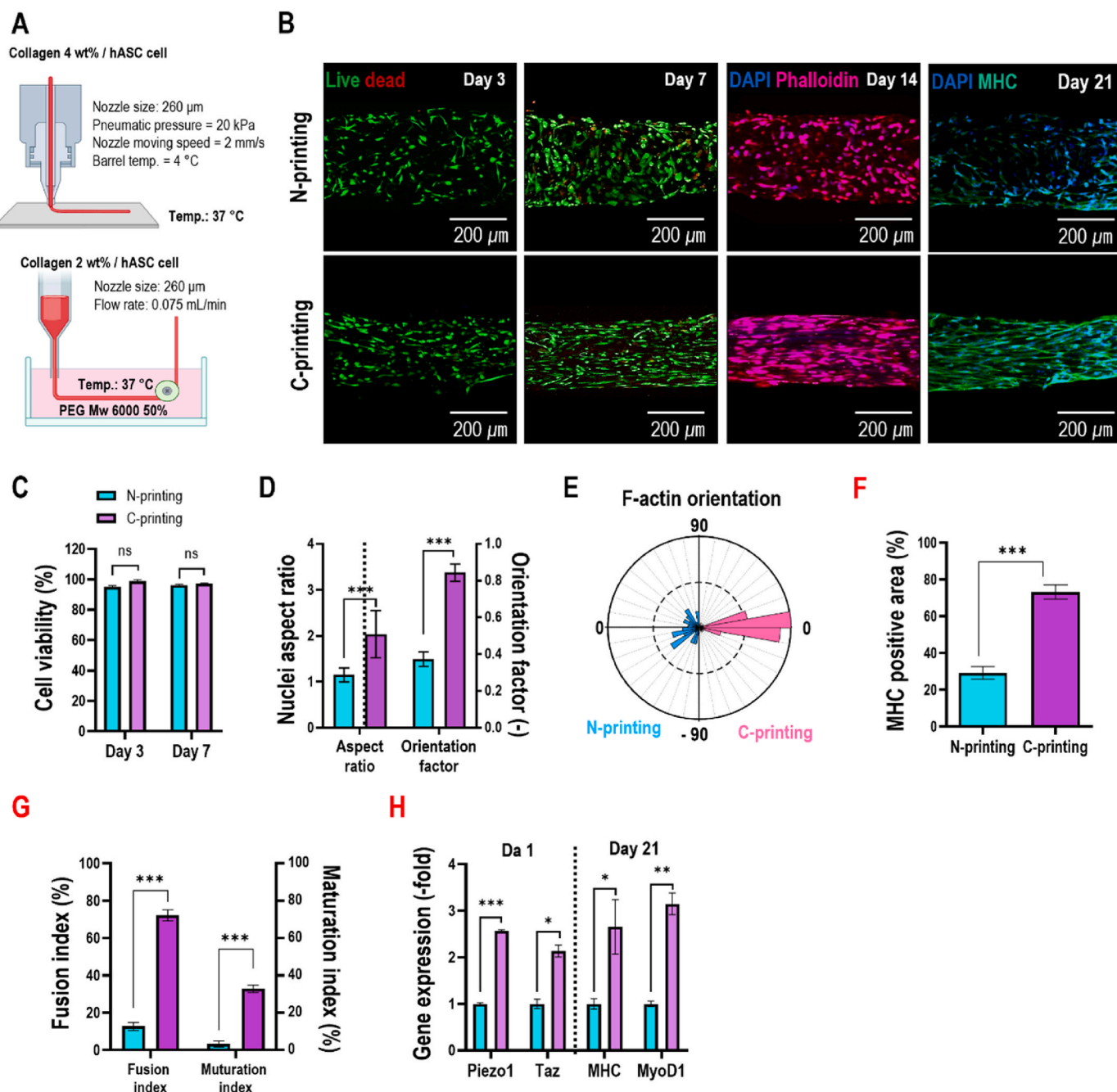
Fig. 6. (**A**) Schematic of conventional (N-printing) and combined (C-printing) bioprinting processes. (**B**) Live/dead images after 3 and 7 days, DAPI/phalloidin staining images after 14 days, and DAPI/MHC staining images after 21 days of culture of hASCs loaded in bioconstructs fabricated using N- or C-printing. Quantification of (**C**) cell viability, (**D**) nuclei aspect ratio and orientation factor, and (**E**) F-actin orientation distribution. Measured (**F**) MHC-positive area, and (**G**) MHC fusion and maturation index of cells cultured in N-printing and C-printing bioconstructs. (**H**) Relative expression levels of Piezo1 and Taz genes after 1 day, and MHC and MyoD1 genes after 21 days for the structures.

Subsequently, various muscle constructs were implanted into the VML defect mice and observed for a duration of four weeks, as depicted in Fig. 7A. During this period, the implanted muscle constructs facilitated muscle regeneration and structural restoration, as shown in Fig. 7B.

Four weeks after the implantation of the muscle constructs, the C-printing group exhibited significantly greater muscle mass than both the VML and N-printing groups, closely matching that of the sham group that did not experience TA loss, as illustrated in Fig. 7C. Additionally, muscle function was assessed using wire hanging (Fig. 7D) and hind limb grip strength tests (Fig. 7E). The hanging durations for the N-printed and wet-spinning groups were as follows: sham, 267.7 ± 4.5 s; VML, 39.7 ±

3.4 s; N-printing group, 146.7 ± 13.5 s; and C-printing group, 199.7 ± 8.4 s. Similarly, the grip strengths for the groups were as follows: sham (79 ± 5.7 g), VML (26 ± 2.4 g), N-printing (40 ± 1.2 g), and C-printing (62 ± 4.6 g). The results clearly indicated an improvement in muscle function in the C-printing group, as evidenced by both the hanging time and grip strength, with a performance equivalent to that of the sham group.

To evaluate the muscle regenerative potential of these constructs at the histological level, cross-sections from each group were stained with hematoxylin and eosin (H&E) and Masson's trichrome (MT) to quantify muscle fiber formation and collagen deposition (Fig. 7F). The C-printed
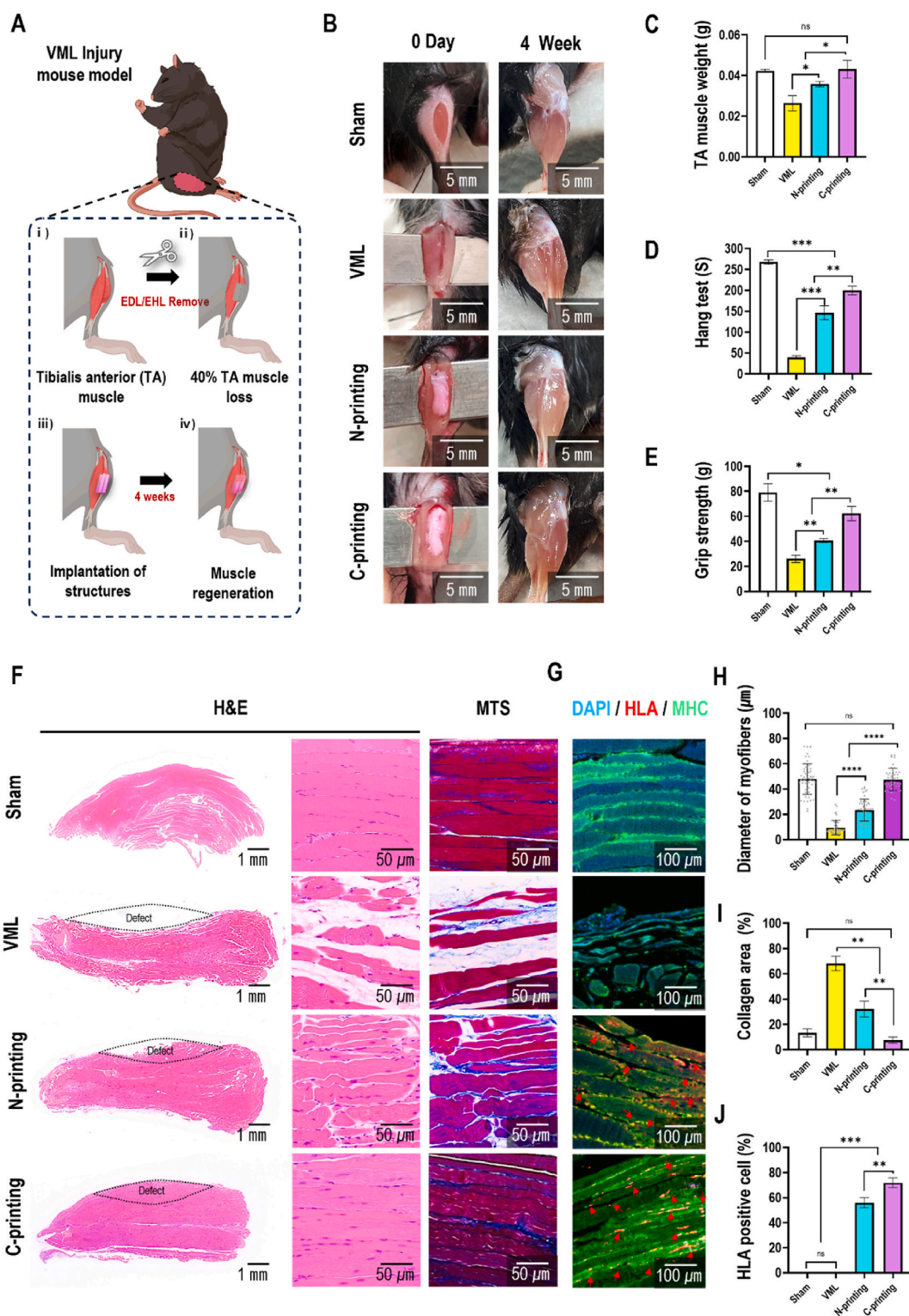
Fig. 7. (**A**) Schematic of implantation of bioconstructs in VML defect in mouse. (**B**) Optical image of TA muscle directly after of implantation and after 4 weeks of implantation. Quantification of (**C**) harvested TA muscle weight, (**D**) hang test duration, and (**E**) grip strength after 4 weeks of bioconstruct implantation. (**F**) H&E and MTS staining images of the TA muscle (black dotted line indicate defect area), and (**G**) immunochemical staining images of DAPI (blue)/HLA (red)/MHC (green). Estimated (**H**) diameter of myofiber, (**I**) collagen area, and (**J**) HLA-positive cells.

structure notably stimulated volumetric muscle regeneration, as observed by the significantly higher number of mature and regenerating muscle fibers than that in the VML and N-printed groups (Fig. 7G).

The measured muscle fiber diameters were as follows: sham, 54.9 ± 8.7 μm; VML, 9.4 ± 5.7 μm; N-printing, 23.4 ± 8.6 μm; and C-printing,

47.5 ± 8.6 μm (Fig. 7H). In terms of fibrotic areas arising from excess collagen deposition, the statistics were as follows: sham (13.4 ± 2.5%), VML (68.2 ± 4.7%), N-printing (32.2 ± 5.1%), and C-printing (7.5 ± 2%), with the VML and control groups displaying significantly higher fibrotic areas (Fig. 7I).

For an in-depth examination of the role of the implanted hASCs within the bioprinted constructs (N-printing and C-printing group) in muscle regeneration, the sectioned TA muscles were subjected to staining for human leukocyte antigen (HLA) and MHC (Fig. 7G, Supplementary Fig. S9). As expected, HLA-expressing myofibers were not observed in the sham and VML groups, whereas HLA was clearly expressed in the implant groups (N- and C-printing groups). This positive HLA and MHC expression indicates that hASCs within the muscle constructs have the capacity to differentiate and contribute to myofiber formation. Furthermore, the numbers of HLA- and MHC-positive cells were significantly higher in the C-printing group than in the control group (Fig. 7J).

During the maturation process of muscle tissue, the immune response to the implanted bioconstruct can be investigated. In our previous work, a collagen bioink comprising human adipose-derived stem cells (hASCs) was employed to regenerate VML defects in C57BL/6 mice [79]. The bioconstruct created using this bioink exhibited a significant reduction in host immune response when contrasted with defect in the mice. The evaluation of immune response was conducted through RNA-sequencing, Gene Set Enrichment Analysis, and co-expression analysis [79]. Based on the results of the previous study, it can be cautiously inferred that the hASCs-laden collagen bioconstruct, when implanted in an *in vivo* mouse model, may elicit relatively diminished immune responses, similar to the results from our previous study.

2.7. Conclusion

Our study proposes a new approach that utilizes PEG-filled submerged printing and stretching to obtain uniaxially aligned cell-laden collagen filaments, targeting the enhancement of muscle tissue regeneration. In contrast to traditional bioprinting methods that often require high collagen concentrations, which can impede cellular activities owing to limited cell-to-cell interactions, we propose the use of a low weight fraction (2 wt%) of collagen to promote efficient cell-to-cell interactions. To address the mechanical challenges associated with low collagen concentration, we incorporated a collagen dehydration process combined with PEG into a submerged bioprinting technique, resulting in the creation of mechanically stable cell filaments with high cell viability. Furthermore, controlled stretching, which promotes mechanotransduction-mediated responses, has been integrated with submerged bioprinting to enhance extracellular matrix remodeling and myogenesis through various *in vitro* cellular activities. *In vivo* experiments conducted using a mouse VML model provide clear evidence of the potential of our approach. This combination of submerged printing, PEG-induced dehydration, and stretching holds promise for fabricating aligned tissue structures such as skeletal muscles and tendons.

3. Experimental section

3.1. Materials

PEG with molecular weights (M_w) of 400 g/mol (PEG-400) and 6000 g/mol (PEG-6000), 1-ethyl-3-(3-dimethylaminopropyl) EDC, and NHS were purchased from Sigma-Aldrich Inc. A porcine-derived type I collagen solution was obtained from MSBio (Seungnam, South Korea).

3.2. Collagen solution preparation and chemical crosslinking and fibrillogenesis of collagen

To identify fibrillogenesis effects under various conditions, 2 wt% collagen was treated with an EDC/NHC solution (200 mM at 37 °C), DMEM solution (37 °C), or PEG-6000 solution (50 wt% at 37 °C) for 8 h. Following the treatment, the collagen structures were rinsed with triple-distilled water.

3.3. Bioink preparation

To obtain a 2 wt% collagen solution, type I collagen was initially dissolved in 0.1 M acetic acid (pH 4.0) at a concentration of 4 wt%. The solution was then neutralized by mixing with an equal volume of 10 M DMEM (Gibco, USA) solution in a 1:1 vol ratio to achieve a final concentration of 2 wt%. The C2C12 murine skeletal muscle cell line (CRL-1772; ATCC, Manassas, VA, USA) at a density of 1×10^7 cells/mL or hASCs (PT-5006; Lonza, Basel, Switzerland) at a density of 1×10^6 cells/mL were loaded into the collagen solution to formulate the bioink.

Additionally, for the bioink used in the N-printing process, a 4 wt% collagen solution was prepared by initially dissolving it in 0.1 M acetic acid at 8 wt%, followed by neutralizing by mixing it thoroughly with an equal volume of 10 M DMEM (Gibco, USA) to achieve a final concentration of 4 wt%. The solution was loaded with hASCs at a density of 1×10^6 cells/mL to form a bioink.

3.4. Fabrication of bioconstructs

To obtain a combined-printed bioconstruct (C-printed), collagen bioink (2 wt%) loaded with hASCs (1×10^6 cells/mL) or C2C12 (1×10^7 cells/mL) was injected into a PEG solution ($M_w = 6000$ g/mol, treatment duration = 5 s, bath temperature = 36 °C) using a syringe pump (Fusion 100; Chemyx, Stafford, TX) at a volumetric flow rate of 0.075 mL/min. Subsequently, collagen fibers were collected using a rotator set at a rotational speed of 7.5 mm/s to conduct wet spinning. To evaluate the effects of wet spinning, collagen bioink loaded with C2C12 cells (1×10^7 cells/mL) was injected into a PEG solution ($M_w = 6000$ g/mol, bath temperature = 36 °C) and collected after being submerged for 5 s.

To obtain normally bioprinted constructs (N-printing) for control purposes, a 4% collagen bioink loaded with hASCs (1×10^6 cells/mL) was 3D bioprinted using a bioprinting system (DTR3-2210T-SG; DASA Robot, South Korea) coupled with a pneumatic dispenser (AD-3000C, Ugin-tech, South Korea). The printing parameters were set as follows: pneumatic pressure = 20 kPa, nozzle moving speed = 2 mm/s, barrel temperature = 4 °C, plate temperature = 37 °C, and nozzle diameter = 260 μm.

3.5. Characterization of collagen struts

Tensile testing was conducted using a UTM (Top-tech, South Korea) to assess the mechanical properties of the various collagen structures. Briefly, collagen struts with a diameter of 3 mm and height of 15 mm were elongated at a constant speed of 0.5 mm/s. The tensile moduli were calculated in the initial linear region of the stress-strain curves.

The morphological properties of the fabricated collagen struts were examined using a microscope (BX FM-32; Olympus) coupled with a digital camera and an SEM (SNE-3000 M; SEC, Inc., South Korea). The images were further analyzed using the ImageJ software (National Institutes of Health, Bethesda, MD, USA) to determine the size of the collagen struts and develop 3D surface mapping.

To evaluate the degree of collagen fibrillation, Fourier transform infrared (FTIR) spectroscopy was performed using an FTIR spectrometer (IRTracer-100; Shimadzu, Kyoto, Japan). FTIR scans were conducted with a mean of 30 scans at 800 to 4000 cm^{-1} at a resolution of 8 cm^{-1}.

Fibrillation analysis of collagen was also conducted using the QI mode of an atomic force microscope (NanoWizard4 Bio-AFM, Bruker, USA). The temperature was maintained at 24 °C during the analysis. High-resolution AFM images of the samples were captured using a Supersharp AFM probe (TESP-SS, Bruker, USA) with a resolution of 9.8 nm/pixel. All AFM images were processed line-by-line, leveled, and analyzed using MountainsSPIP software (version 9, Digital Surf, France).

3.6. In vitro cell culture

The fabricated collagen constructs loaded with C2C12 myoblasts

were placed in six-well culture plates and cultured in high-glucose Dulbecco's modified Eagle's medium (LM 001–05; Welgene, Gyeongsan-si, South Korea) supplemented with 1% penicillin/streptomycin (PS) (Antimycotic; Thermo-Fisher Scientific, USA) and 10% fetal bovine serum (FBS, Gemini Bio-Products, USA). To accelerate myogenic activity in C2C12 cells, high-glucose DMEM containing 2% horse serum (H1270; Sigma Aldrich St Louis, USA) and 1% penicillin was used. For *in vitro* cellular culture of the bioconstructs loaded with hASCs, the samples were cultured in low-glucose Dulbecco's modified Eagle's medium (LM 001–06; Welgene, Gyeongsan-si, South Korea) containing 1% penicillin and 10% FBS. To induce the myogenesis of the hASCs, the fabricated construct was cultured in myogenic medium consisting of low-glucose DMEM containing 10% FBS, 5% horse serum, 0.1 μM dexamethasone (D4902; Sigma Aldrich St Louis, USA), 50 μM hydrocortisone (H0888; Sigma Aldrich St Louis, USA), and 1% penicillin. The bioconstructs were cultured in 5% CO_2 at 37 °C, and the medium was changed every 2 days.

To analyze the viability of cells, 0.15 mM calcein AM and 2 mM ethidium homodimer-1 (Thermo Fisher Scientific, USA) were used to stain the samples for 1 h at 37 °C. Stained cell-laden structures were visualized using a Zeiss confocal microscope. Cell viability was calculated by quantifying live/dead staining using ImageJ software.

The morphology of cells cultured in various collagen structures was evaluated using DAPI/phalloidin staining. Briefly, the nuclei and filamentous actin (F-actin) were fixed in 0.7% paraformaldehyde (252549; Sigma-Aldrich) for 1 h and permeabilized with 0.1% Triton X-100 (T8787; Sigma-Aldrich) for 20 min. The structures were submerged in distilled water consisting of diamidino-2-phenylinodole (DAPI) (dilution ratio = 1:100 in PBS; Invitrogen, Carlsbad, USA) and Alexa Fluor fluorescein phalloidin (red) (dilution ratio = 1:100 in PBS; Invitrogen) for 90 min. Confocal microscopy was used to visualize the nuclei and F-actin, and the images were further evaluated using ImageJ software to calculate the orientation factor [(90°-FWHM)/90°, where FWHM is the full width at half maximum] and the nucleus aspect ratio.

3.7. Immunofluorescence staining

To visualize the myogenesis, the filaments were rinsed thrice with PBS, fixed using 3.7% formaldehyde solution in PBS overnight at 4 °C, blocked with 2% bovine serum albumin (BSA; Sigma-Aldrich) for 2 h at 37 °C, and permeabilized with 2% Triton X-100 (Cytiva Hyclone Laboratories) for another 2 h at 37 °C. Thereafter, the cells contained in the collagen-filaments were incubated overnight at 4 °C with primary antibodies against antiMF20 (5 mg/mL; Developmental Studies Hybridoma Bank, Iowa City, IA, USA). Rinsing with PBS was performed twice at each step. The cell-laden filaments were then stained with secondary antibodies conjugated to anti-mouse Alexa Fluor 488 (1:50 in PBS; Invitrogen) for 4 h. The stained samples were counterstained with 5 mM DAPI. A Carl Zeiss confocal microscope was used to visualize the stained cells, followed by quantification of MHC orientation, MHC fusion, and maturation index using ImageJ software.

3.8. Real-time polymerase chain reaction

Various myogenic and mechanotransduction-related genes were normalized to the housekeeping gene glyceraldehyde-3-phosphate dehydrogenase (GAPDH). RNA was extracted from the cultured samples using the TRI reagent (Sigma-Aldrich), and its purity and concentration were assessed using a spectrophotometer (FLX800T; Biotek, Winooski, VT, USA). Complementary DNA (cDNA) was synthesized from the purified RNA treated with RNase-free DNase using a reverse transcription system. The Thunderbird SYBR qPCR mix (Toyobo, Osaka, Japan) was used for the SYBR Green assay, and the samples were analyzed using a StepOnePlus Real-Time PCR System (Applied Biosystems, Foster City, CA, USA) following the manufacturer's instructions. The primer sequences used for PCR amplification are listed in Supplementary Tables 3 and 4

3.9. VML defect injury model

To further elucidate the muscle regenerative potential, the fabricated structures were evaluated using a volumetric muscle loss (VML) defect model in mice. The VML defects were generated in 10-week-old male C57BL/6 mice (DooYeol Biotech, Inc., Seoul, Korea). All animal procedures were performed according to the protocol (GIST-2023-017) approved by the Animal Care and Use Committee of the Gwangju Institute of Science and Technology (GIST) of South Korea. First, the mice were anesthetized with 3% isoflurane, followed by an incision of the skin of the lower left leg, where the muscle was separated from the fascia. The extensor digitorum longus and extensor hallucis longus muscles were removed to prevent compensatory hypertrophy in response to the VML injury, and approximately 40% of the TA muscles were excised and weighed. The following equation: y (g) = 0.0017 × body weight (g) – 0.0716 [77] was used to calculate the TA muscle weight of each mouse (Supplementary Table 3). The collagen structures were implanted into the TA defect site, closed, and sutured to the fascia and skin. Four groups were utilized at 4-week time points (12 animals in total, n = 3/group): (i) control (sham), (ii) non-treated (defect), (iii) conventionally bioprinted by N-printing, and (iv) C-printing. Prior to implantation, the cell-laden constructs were cultured in growth medium for one day. Cell-laden constructs (1×10^6 cells/mL) were fabricated with the dimensions of $2 \times 4 \times 1.5$ mm^3.

3.10. Muscle functional tests

In vivo muscle function was assessed in live mice using the hanging test and grip-strength evaluation. Briefly, the time taken by the mice to fall from the rod (hang test) was measured five times during each test, and the maximum latency was set to 300 s, at which point the test was terminated. The grip strength of mice was determined using a previously described method [78]. After 4-weeks of implantation, each mouse was placed in a pull-grid assembly coupled with a grip strength meter (BIO-G53, BIOSEB, FL, USA). To measure the maximal grip strength, each mouse was pulled parallel to the grid. The measurement was repeated three times per mouse with 5 min time intervals between repetitions. Finally, the TA muscle of each lower leg was collected and weighed.

3.11. Histological and immunofluorescence staining

For histological evaluation, TA muscle samples harvested from mice after 4 weeks were fixed with 4% paraformaldehyde at 25 °C for 24 h. The samples were then paraffin-embedded and sectioned into 5 μm sections. Subsequently, deparaffinized sections were stained with hematoxylin and eosin (H&E) and MT for histological analysis. The diameters of the muscle fibers and collagen areas were quantified using ImageJ software.

Additionally, the deparaffinized sections were treated with mouse anti-MHC (1:50 dilution; Santa Cruz Biotechnology, Dallas, TX, USA) and rabbit anti-human leukocyte antigen (HLA; species reactivity: human) (1:50 dilution; Abcam, Cambridge, UK). The muscle sections were then rinsed with PBS three times, immersed in Alexa Fluor 488-conjugated anti-rabbit (1:200 dilution; Abcam) and Alexa Fluor 594-conjugated anti-mouse (1:200 dilution; Abcam) secondary antibodies for 30 min, and counterstained with DAPI. Stained sections were visualized using a confocal microscope. The percentage of HLA + myofibers was quantified using ImageJ software in a blinded manner.

3.12. Statistical analysis

All data are presented as mean ± standard deviation (SD). For normally distributed continuous variables with three or more treatment groups, one-way analysis of variance (ANOVA) was conducted, followed by Tukey's post-hoc test for pairwise comparisons. Student's *t*-test was

performed for comparisons between two groups. Statistical analyses were performed using SPSS for Windows (version 18.0; SPSS, Chicago, IL, USA), and statistical significance was defined as $p^* < 0.05$, $p^{**} < 0.01$, and $p^{***} < 0.001$.

Data availability

The data in this work are available in the manuscript or Supplementary Information, or available from the corresponding author upon reasonable request.

Ethics approval and consent to participate

All animal procedures were performed according to the protocol (GIST-2023-017) approved by the Animal Care and Use Committee of the Gwangju Institute of Science and Technology (GIST) of South Korea.

Declaration of interests

The authors (JuYeon Kim, Hyeongjin Lee, Gyudo Lee, Dongryeol Ryu, and GeunHyung Kim) declare that they have no known competing financial interests or personal relationships that could have appeared to influence the work reported in this paper.

CRediT authorship contribution statement

JuYeon Kim: Methodology, Investigation, Formal analysis, Data curation, Conceptualization. **Hyeongjin Lee:** Investigation, Data curation, Conceptualization. **Gyudo Lee:** Investigation, Formal analysis. **Dongryeol Ryu:** Formal analysis, Data curation. **GeunHyung Kim:** Writing – review & editing, Writing – original draft, Supervision, Project administration, Investigation, Formal analysis, Data curation, Conceptualization.

Acknowledgments

Appendix A. Supplementary data

Supplementary data to this article can be found online at https://doi.org/10.1016/j.bioactmat.2024.02.020.

References

[1] B.J. Kwee, D.J. Mooney, Biomaterials for skeletal muscle tissue engineering, Curr. Opin. Biotechnol. 47 (2017) 16–22, https://doi.org/10.1016/j.copbio.2017.05.003.

[2] R. Dong, P.X. Ma, B. Guo, Conductive biomaterials for muscle tissue engineering, Biomaterials 229 (2020) 119584, https://doi.org/10.1016/j.biomaterials.2019.119584.

[3] J.H. Kim, I. Kim, Y.-J. Seol, I.K. Ko, J.J. Yoo, A. Atala, S.J. Lee, Neural cell integration into 3D bioprinted skeletal muscle constructs accelerates restoration of muscle function, Nat. Commun. 11 (2020) 1025, https://doi.org/10.1038/s41467-020-14930-9.

[4] H. Lee, W. Kim, J. Lee, K.S. Park, J.J. Yoo, A. Atala, G.H. Kim, S.J. Lee, Self-aligned myofibers in 3D bioprinted extracellular matrix-based construct accelerate skeletal muscle function restoration, Appl. Phys. Rev. 8 (2) (2021), https://doi.org/10.1063/5.0039639.

[5] H. Hwangbo, H. Lee, E.J. Jin, Y. Jo, J. Son, H.M. Woo, D. Ryu, G.H. Kim, Photosynthetic Cyanobacteria can clearly Induce efficient muscle tissue regeneration of bioprinted cell-constructs, Adv. Funct. Mater. 33 (10) (2023) 2209157, https://doi.org/10.1002/adfm.202209157.

[6] N. Ashammakhi, S. Ahadian, C. Xu, H. Montazerian, H. Ko, R. Nasiri, N. Barros, A. Khademhosseini, Bioinks and bioprinting technologies to make heterogeneous and biomimetic tissue constructs, Mater. Today Bio 1 (2019) 100008, https://doi.org/10.1016/j.mtbio.2019.100008.

[7] J. Lee, H. Lee, E.-J. Jin, D. Ryu, G.H. Kim, 3D bioprinting using a new photo-crosslinking method for muscle tissue restoration, NPJ Regen. Med. 8 (1) (2023) 18, https://doi.org/10.1038/s41536-023-00292-5.

[8] A. Schwab, R. Levato, M. D'Este, S. Piluso, D. Eglin, J. Malda, Printability and shape fidelity of bioinks in 3D bioprinting, Chem. Rev. 120 (19) (2020) 11028–11055, https://doi.org/10.1021/acs.chemrev.0c00084.

[9] ASTM WK74668, New Guide for Bioinks and Biomaterial Inks Used in Bioprinting Tissue-Engineered Medical Products, 2020. West Conshohocken, PA, https://www.astm.org/workitem-wk74668.

[10] F. Liu, R. Quan, C. Vyas, E. Aslan, Hybrid biomanufacturing systems applied in tissue regeneration, Int. J. Bioprinting 9 (2023) 1, https://doi.org/10.18063/ijb.v9i1.646.

[11] D.A. Foyt, M.D. Norman, T.T. Yu, E. Gentleman, Exploiting advanced hydrogel technologies to address key challenges in regenerative medicine, Adv. Healthcare Mater. 7 (2018) 1700939, https://doi.org/10.1002/adhm.201700939.

[12] W.L. Ng, J.M. Lee, M. Zhou, Y.W. Chen, K.X.A. Lee, W.Y. Yeong, Y.E. Shen, Vat polymerization-based bioprinting—process, materials, applications and regulatory challenges, Biofabrication 12 (2020) 022001, https://doi.org/10.1088/1758-5090/ab6034.

[13] J.A. Smith, E. Mele, Electrospinning and additive manufacturing: adding three-dimensionality to electrospun scaffolds for tissue engineering, Front. Bioeng. Biotechnol. 9 (2021) 674738, https://doi.org/10.3389/fbioe.2021.674738.

[14] M.S. Kang, S.H. Lee, W.J. Park, J.E. Lee, B. Kim, D.W. Han, Advanced techniques for skeletal muscle tissue engineering and regeneration, Bioengineering 7 (2020) 99, https://doi.org/10.3390/bioengineering7030099.

[15] J.W. Jung, J.S. Lee, D.W. Cho, Computer-aided multiple-head 3D printing system for printing of heterogeneous organ/tissue constructs, Sci. Rep. 6 (2016) 21685, https://doi.org/10.1038/srep21685.

[16] I.T. Ozbolat, H. Chen, Y. Yu, Development of 'Multi-arm Bioprinter' for hybrid biofabrication of tissue engineering constructs, Robot. Comput. Integrated Manuf. 30 (2014) 295–304, https://doi.org/10.1016/j.rcim.2013.10.005.

[17] T.J. Hinton, Q. Jallerat, R.N. Palchesko, J.H. Park, M.S. Grodzicki, H.-J. Shue, M. H. Ramadan, A.R. Hudson, A.W. Feinberg, Three-dimensional printing of complex biological structures by freeform reversible embedding of suspended hydrogels, Sci. Adv. 1 (2015) e1500758, https://doi.org/10.1126/sciadv.1500758.

[18] E. Mirdamadi, J.W. Tashman, D.J. Shiwarski, R.N. Palchesko, A.W. Feinberg, FRESH 3D bioprinting a full-size model of the human heart, ACS Biomater. Sci. Eng. 6 (2020) 6453–6459, https://doi.org/10.1021/acsbiomaterials.0c01133.

[19] A. Lee, A.R. Hudson, D.J. Shiwarski, J.W. Tashman, T.J. Hinton, S. Yerneni, J. M. Bliley, P.G. Campbell, A.W. Feinberg, 3D bioprinting of collagen to rebuild components of the human heart, Science 365 (2019) 482–487, https://doi.org/10.1126/science.aav9051.

[20] Y. Yanagi, K. Nakayama, T. Taguchi, S. Enosawa, T. Tamura, K. Yoshimaru, T. Matsuura, M. Hayashida, K. Kohashi, Y. Oda, T. Yamaza, E. Kobayashi, In vivo and ex vivo methods of growing a liver bud through tissue connection, Sci. Rep. 7 (2017) 14085, https://doi.org/10.1038/s41598-017-14542-2.

[21] D. Murata, Y. Kunitomi, K. Harada, S. Tokunaga, S. Takao, K. Nakayama, Osteochondral regeneration using scaffold-free constructs of adipose tissue-derived mesenchymal stem cells made by a bio three-dimensional printer with a needle-array in rabbits, Regen. Ther. 15 (2020) 77–89, https://doi.org/10.1016/j.reth.2020.05.004.

[22] Y. Zhang, B. Wang, J. Hu, T. Yin, T. Yue, N. Liu, Y. Liu, 3D composite bioprinting for fabrication of artificial biological tissues, Int. J. Bioprint. 7 (2021) 299, https://doi.org/10.18063/ijb.v7i1.299.

[23] M. Hospodiuk, M. Dey, D. Sosnoski, I.T. Ozbolat, The bioink: a comprehensive review on bioprintable materials, Biotechnol. Adv. 35 (2) (2017) 217–239, https://doi.org/10.1016/j.biotechadv.2016.12.006.

[24] Ö. Yildirim, A. Arslan-Yildiz, Development of a hydrocolloid bio-ink for 3D bioprinting, Biomater. Sci. 10 (23) (2022) 6707–6717, https://doi.org/10.1039/D2BM01184K.

[25] M.A. Omobono, X. Zhao, M.A. Furlong, C.H. Kwon, T.J. Gill, M.A. Randolph, R. W. Redmond, Enhancing the stiffness of collagen hydrogels for delivery of encapsulated chondrocytes to articular lesions for cartilage regeneration, J. Biomed. Mater. Res. 103 (4) (2015) 1332–1338, https://doi.org/10.1002/jbm.a.35266.

[26] A. Oryan, A. Kamali, A. Moshiri, H. Baharvand, H. Daemi, Chemical crosslinking of biopolymeric scaffolds: current knowledge and future directions of crosslinked engineered bone scaffolds, Int. J. Biol. Macromol. 107 (2018) 678–688, https://doi.org/10.1016/j.ijbiomac.2017.08.184.

[27] B. Ma, X. Wang, C. Wu, Crosslinking strategies for preparation of extracellular matrix-derived cardiovascular scaffolds, J. Chang. Regen. Biomater 11 (1) (2014) 81–89, https://doi.org/10.1093/rb/rbu009.

[28] L.H.H. Olde Damink, P.J. Dijkstra, M.J.A. Van Luyn, P.B. Van Wachem, P. Nieuwenhuis, J. Feijen, Glutaraldehyde as a crosslinking agent for collagen-based biomaterials, J. Mater. Sci. Mater. Med. 6 (1995) 460–472, https://doi.org/10.1007/BF00123371.

[29] C. Gögele, J. Hahn, C. Elschner, A. Breier, M. Schröpfer, L. Prade, M. Meyer, G. Schulze-Tanzil, Enhanced growth of lapine anterior cruciate ligament-derived fibroblasts on scaffolds embroidered from poly(l-lactide-co-ε-caprolactone) and polylactic acid threads functionalized by fluorination and hexamethylene diisocyanate cross-linked collagen foams, Int. J. Mol. Sci. 21 (2020) 1132, https://doi.org/10.3390/ijms21031132.

[30] R.M. Hassan, Novel synthesis of natural cation exchange resin by crosslinking the sodium alginate as a natural polymer with 1,6-hexamethylene diisocyanate in inert

solvents: characteristics and applications, Int. J. Biol. Macromol. 184 (2021) 926–935, https://doi.org/10.1016/j.ijbiomac.2021.06.147.

[31] G. Montalbano, G. Borciani, G. Cerqueni, C. Licini, F. Banche-Niclot, D. Janner, S. Sola, S. Fiorilli, M. Mattioli-Belmonte, G. Ciapetti, Collagen hybrid formulations for the 3D printing of nanostructured bone scaffolds: an optimized genipin-crosslinking strategy, Nanomaterials 10 (2020) 1681, https://doi.org/10.3390/nano10091681.

[32] Z. Wang, H. Liu, W. Luo, T. Cai, Z. Li, Y. Liu, W. Gao, Q. Wan, X. Wang, J. Wang, Regeneration of skeletal system with genipin crosslinked biomaterials, J. Tissue Eng. 11 (2020) 2041731420974861, https://doi.org/10.1177/2041731420974861.

[33] C. Yang, Enhanced physicochemical properties of collagen by using EDC/NHS-crosslinking, Bull. Mater. Sci. 35 (2012) 913–918, https://doi.org/10.1007/s12034-012-0376-5.

[34] H. Goodarzi, K. Jadidi, S. Pourmotabed, E. Sharifi, H. Aghamollaei, Preparation and in vitro characterization of cross-linked collagen–gelatin hydrogel using EDC/NHS for corneal tissue engineering applications, Int. J. Biol. Macromol. 126 (2019) 620–632, https://doi.org/10.1016/j.ijbiomac.2018.12.125.

[35] M.H. Cumming, A.R. Leonard, D.S. LeCorre-Bordes, K. Hofman, Intra-fibrillar citric acid crosslinking of marine collagen electrospun nanofibres, Int. J. Biol. Macromol. 114 (2018) 874–881.

[36] M. Andonegi, K. de la Caba, P. Guerrero, Effect of citric acid on collagen sheets processed by compression, Food Hydrocolloids 100 (2020) 105427, https://doi.org/10.1016/j.ijbiomac.2018.03.180.

[37] I. Prasertsung, S. Damrongsakkul, N. Saito, Crosslinking of gelatin solutions induced by pulsed electrical discharges in solutions, Plasma Process, Polym 10 (2013) 792–797, https://doi.org/10.1002/ppap.201200148.

[38] A. Liguori, A. Bigi, V. Colombo, M.L. Focarete, M. Gherardi, C. Gualandi, M. C. Oleari, S. Panzavolta, Atmospheric pressure non-equilibrium plasma as a green tool to crosslink gelatin nanofibers, Sci. Rep. 6 (2016) 38542, https://doi.org/10.1038/srep38542.

[39] N. Davidenko, D.V. Bax, C.F. Schuster, R.W. Farndale, S.W. Hamaia, S.M. Best, R. E. Cameron, Optimisation of UV irradiation as a binding site conserving method for crosslinking collagen-based scaffolds, J. Mater. Sci. Mater. Med. 27 (2016) 1–17, https://doi.org/10.1007/s10856-015-5627-9.

[40] K.S. Weadock, E.J. Miller, L.D. Bellincampi, J.P. Zawadsky, M. Dunn, Physical crosslinking of collagen fibers: comparison of ultraviolet irradiation and dehydrothermal treatment, J. Biomed. Mater. Res. 29 (1995) 1373–1379, https://doi.org/10.1002/jbm.820291108.

[41] D.V. Bax, N. Davidenko, S.W. Hamaia, R.W. Farndale, S.M. Best, R.E. Cameron, Impact of UV- and carbodiimide-based crosslinking on the integrin-binding properties of collagen-based materials, Acta Biomater. 100 (2019) 280–291, https://doi.org/10.1016/j.actbio.2019.09.046.

[42] S. Nagaraj, S. Easwaramoorthi, J.R. Rao, P. Thanikaivelan, Probing visible light induced photochemical stabilization of collagen in green solvent medium, Int. J. Biol. Macromol. 131 (2019) 779–786, https://doi.org/10.1016/j.ijbiomac.2019.03.109.

[43] H. Xu, J. Casillas, S. Krishnamoorthy, C. Xu, Effects of Irgacure 2959 and lithium phenyl-2, 4, 6-trimethylbenzoylphosphinate on cell viability, physical properties, and microstructure in 3D bioprinting of vascular-like constructs, Biomed. Mater. 15 (5) (2020) 055021, https://doi.org/10.1088/1748-605X/ab954e.

[44] X.H. Ma, Y. Noishiki, Y. Yamane, Y. Iwai, D. Marato, A. Matsumoto, Thermal cross-linking for biologically degradable materials, Preliminary report, Am. Soc. Artif. Intern. Organs J. 42 (1996) M866–M871, https://doi.org/10.1097/00002480-199609000-00115.

[45] J.W. Drexler, H.M. Powell, Dehydrothermal crosslinking of electrospun collagen, Tissue Eng. C Methods 17 (2010) 9–17, https://doi.org/10.1089/ten.TEC.2009.0754.

[46] S. Cheng, W. Wang, Y. Li, G. Gao, K. Zhang, J. Zhou, Z. Wu, Cross-linking and film-forming properties of transglutaminase-modified collagen fibers tailored by denaturation temperature, Food Chem. 271 (2019) 527–535, https://doi.org/10.1016/j.foodchem.2018.07.223.

[47] Y. Liu, R. Weng, W. Wang, X. Wei, J. Li, X. Chen, Y. Liu, F. Lu, Y. Li, Tunable physical and mechanical properties of gelatin hydrogel after transglutaminase crosslinking on two gelatin types, Int. J. Biol. Macromol. 162 (2020) 405–413, https://doi.org/10.1016/j.ijbiomac.2020.06.185.

[48] L.H.H. Olde Damink, P.J. Dijkstra, M.J.A. Van Luyn, P.B. Van Wachem, P. Nieuwenhuis, J. Feijen, Crosslinking of dermal sheep collagen using hexamethylene diisocyanate, J. Mater. Sci. Mater. Med. 6 (1995) 429–434, https://doi.org/10.1007/BF00120286.

[49] C. Liu, Y. Zhou, M. Sun, Q. Li, L. Dong, L. Ma, K. Cheng, W. Weng, M. Yu, H. Wang, Light-induced cell alignment and harvest for anisotropic cell sheet technology, ACS Appl. Mater. Interfaces 9 (42) (2017) 36513–36524, https://doi.org/10.1021/acsami.7b07202.

[50] X. Shi, S. Ostrovidov, Y. Zhao, X. Liang, M. Kasuya, K. Kurihara, K. Nakajima, H. Bae, H. Wu, A. Khademhosseini, Microfluidic spinning of cell-responsive grooved microfibers, Adv. Funct. Mater. 25 (15) (2015) 2250–2259, https://doi.org/10.1002/adfm.201404531.

[51] J.P. Armstrong, J.L. Puetzer, A. Serio, A.G. Guex, M. Kapnisi, A. Breant, Y. Zong, V. Assal, S.C. Skaalure, O. King, Engineering anisotropic muscle tissue using acoustic cell patterning, Adv. Mater. 30 (43) (2018) 1802649, https://doi.org/10.1002/adma.201802649.

[52] K.J. De France, K.G. Yager, K.J. Chan, B. Corbett, E.D. Cranston, T. Hoare, Injectable anisotropic nanocomposite hydrogels direct in situ growth and alignment of myotubes, Nano Lett. 17 (10) (2017) 6487–6495, https://doi.org/10.1021/acs.nanolett.7b03600.

[53] G.H. Yang, W. Kim, J. Kim, G. Kim, A skeleton muscle model using GelMA-based cell-aligned bioink processed with an electric-field assisted 3D/4D bioprinting, Theranostics 11 (1) (2021) 48, https://doi.org/10.7150/thno.50794.

[54] W. Kim, H. Lee, C.K. Lee, J.W. Kyung, S.B. An, I.B. Han, G.H. Kim, A bioprinting process supplemented with in situ electrical stimulation directly induces significant myotube formation and myogenesis, Adv. Funct. Mater. 31 (51) (2021) 2105170, https://doi.org/10.1002/adfm.202105170.

[55] W. Kim, G. Kim, Bioprinting 3D muscle tissue supplemented with endothelial-spheroids for neuromuscular junction model, Appl. Phys. Rev. 10 (3) (2023), https://doi.org/10.1063/5.0152924.

[56] A. Johansson, P. Kollman, S. Rothenberg, J. McKelvey, Hydrogen bonding ability of the amide group, J. Am. Chem. Soc. 96 (12) (1974) 3794–3800, https://doi.org/10.1021/ja00819a013.

[57] M. Madaghiele, E. Calò, L. Salvatore, V. Bonfrate, D. Pedone, M. Frigione, A. Sannino, Assessment of collagen crosslinking and denaturation for the design of regenerative scaffolds, J. Biomed. Mater. Res. 104 (1) (2016) 186–194, https://doi.org/10.1002/jbm.a.35554.

[58] G. Liu, Y. Li, L. Yang, Y. Wei, X. Wang, Z. Wang, L. Tao, Cytotoxicity study of polyethylene glycol derivatives, RSC Adv. 7 (30) (2017) 18252–18259, https://doi.org/10.1039/C7RA00861A.

[59] M. Fischer, P. Rikeit, P. Knaus, C. Coirault, YAP-mediated mechanotransduction in skeletal muscle, Front. Physiol. 7 (2016) 41, https://doi.org/10.3389/fphys.2016.00041.

[60] K. Hölzl, S. Lin, L. Tytgat, S. Van Vlierberghe, L. Gu, A. Ovsianikov, Bioink properties before, during and after 3D bioprinting, Biofabrication 8 (3) (2016) 032002, https://doi.org/10.1088/1758-5090/8/3/032002.

[61] S. Das, F. Pati, Y.-J. Choi, G. Rijal, J.-H. Shim, S.W. Kim, A.R. Ray, D.-W. Cho, S. Ghosh, Bioprintable, cell-laden silk fibroin–gelatin hydrogel supporting multilineage differentiation of stem cells for fabrication of three-dimensional tissue constructs, Acta Biomater. 11 (2015) 233–246, https://doi.org/10.1016/j.actbio.2014.09.023.

[62] S. Kreger, B. Bell, J. Bailey, E. Stites, J. Kuske, B. Waisner, S. Voytik-Harbin, Polymerization and matrix physical properties as important design considerations for soluble collagen formulations, Biopolymers 93 (8) (2010) 690–707, https://doi.org/10.1002/bip.21431.

[63] M.G. McCoy, B.R. Seo, S. Choi, C. Fischbach, Collagen I hydrogel microstructure and composition conjointly regulate vascular network formation, Acta Biomater. 44 (2016) 200–208, https://doi.org/10.1016/j.actbio.2016.08.028.

[64] C. Haynl, E. Hofmann, K. Pawar, S. Förster, T. Scheibel, Microfluidics-produced collagen fibers show extraordinary mechanical properties, Nano Lett. 16 (9) (2016) 5917–5922, https://doi.org/10.1021/acs.nanolett.6b02828.

[65] Y.A. Nashchekina, A. Starostina, N. Trusova, M.Y. Sirotkina, A. Lihachev, A. Nashchekin, Molecular and fibrillar structure collagen analysis by FTIR spectroscopy, J. Phys. Conf. Ser. (2020) 012053, https://doi.org/10.1088/1742-6596/1697/1/012053.

[66] B. Sun, The mechanics of fibrillar collagen extracellular matrix, Cell Rep. Phys. Sci. 2 (8) (2021), https://doi.org/10.1016/j.xcrp.2021.100515.

[67] M.C. Branco, F. Nettesheim, D.J. Pochan, J.P. Schneider, N.J. Wagner, Fast dynamics of semiflexible chain networks of self-assembled peptides, Biomacromolecules 10 (6) (2009) 1374–1380, https://doi.org/10.1021/bm801396e.

[68] T.H. Qazi, D.J. Mooney, M. Pumberger, S. Geissler, G.N. Duda, Biomaterials based strategies for skeletal muscle tissue engineering: existing technologies and future trends, Biomaterials 53 (2015) 502–521, https://doi.org/10.1016/j.biomaterials.2015.02.110.

[69] M. Yeo, G. Kim, Optimal size of cell-laden hydrogel cylindrical struts for enhancing the cellular activities and their application to hybrid scaffolds, J. Mater. Chem. B 2 (39) (2014) 6830–6838, https://doi.org/10.1039/C4TB00785A.

[70] B. Suki, H. Parameswaran, E. Imsirovic, E. Bartolák-Suki, Regulatory roles of fluctuation-driven mechantransduction in cell function, Physiol. 31 (2016) 346–358, https://doi.org/10.1152/physiol.00051.2015.

[71] E.R. Hinkle, R.E. Blue, Y.H. Tsai, M. Combs, Jacquelyn, A.R. Coffey, A.M. Boriek, J. M. Taulor, J.S. Parker, J. Giudice, Stretching muscle cells induces transcriptional and splicing transitions and changes in SR proteins, Commun. Biol. 5 (2022) 987, https://doi.org/10.1038/s42003-022-03915-7.

[72] K.E. Scott, S.I. Fraley, P. Rangamani, A spatial model of YAP/TAZ signaling reveals how stiffness, dimensionality, and shape contribute to emergent outcomes, Proc. Natl. Acad. Sci. USA 118 (2021) e2021571118, https://doi.org/10.1038/s42003-022-03915-7.

[73] L. LeBlanc, N. Ramirez, Context-dependent roles of YAP/TAZ in stem cell fates and cancer, Cell. Mol. Life Sci. 78 (2021) 4201–4219, https://doi.org/10.1007/s00018-021-03781-2.

[74] N. Ma, D. Chen, J.-H. Lee, P. Kuri, E.B. Hernandez, J. Kocan, H. Mahmood, E. D. Tichy, P. Rompolas, F. Mourkioti, Piezo1 regulates the regenerative capacity of skeletal muscles via orchestration of stem cell morphological states, Sci. Adv. 8 (11) (2022), https://doi.org/10.1126/sciadv.abn0485 eabn0485.

[75] G.H. Park, H. Jeong, M.G. Jeong, E.J. Jang, M.A. Bae, Y.L. Lee, N.J. Kim, J. H. Hong, E.S. Hwang, Novel TAZ modulators enhance myogenic differentiation and muscle regeneration, Br. J. Pharmacol. 171 (17) (2014) 4051–4061, https://doi.org/10.1111/bph.12755.

[76] J. Kim, H. Lee, E.J. Jin, Y. Jo, B.E. Kang, D. Ryu, G. Kim, A microfluidic device to fabricate one-step cell bead-laden hydrogel struts for tissue engineering, Small 18 (2022) 2106487, https://doi.org/10.1002/smll.202106487.

[77] X. Wu, B.T. Corona, X. Chen, T.J. Walters, A standardized rat model of volumetric muscle loss injury for the development of tissue engineering therapies, BioResearch Open Access 1 (6) (2012) 280–290, https://doi.org/10.1089/biores.2012.0271.

[78] D. Ryu, H. Zhang, E.R. Ropelle, V. Sorrentino, D.A. Mázala, L. Mouchiroud, P. L. Marshall, M.D. Campbell, A.S. Ali, G.M. Knowels, NAD+ repletion improves muscle function in muscular dystrophy and counters global PARylation, Sci. Transl. Med. 8 (361) (2016), https://doi.org/10.1126/scitranslmed.aaf5504, 361ra139-361ra139.